HHS Public Access

Author manuscript

IEEE Trans Instrum Meas. Author manuscript; available in PMC 2020 February 01.

Published in final edited form as:

IEEE Trans Instrum Meas. 2019 February ; 68(2): 493–501. doi:10.1109/TIM.2018.2851458.

Magnetic Source Imaging Using a Pulsed Optically Pumped Magnetometer Array

Amir Borna[1], **Tony R. Carter**[1], **Paul DeRego**[2], **Conrad D. James**[1], **Peter D. D. Schwindt**[1]

[1]Sandia National Laboratories, PO Box 5800, Albuquerque, NM 87185-1082, USA

[2]Kansas City National Security Campus, 2450 Alamo Ave SE, Albuquerque, NM 87106

Abstract

We have developed a pulsed optically pumped magnetometer (OPM) array for detecting magnetic field maps originated from an arbitrary current distribution. The presented magnetic source imaging (MSI) system features 24 OPM channels, has a data rate of 500 S/s, a sensitivity of 0.8 $pT/\sqrt{Hz}$, and a dynamic range of 72 dB. We have employed our pulsed- OPM MSI system for measuring the magnetic field map of a test coil structure. The coils are moved across the array in an indexed fashion to measure the magnetic field over an area larger than the array. The captured magnetic field maps show excellent agreement with the simulation results. Assuming a 2D current distribution, we have solved the inverse problem, using the measured magnetic field maps, and the reconstructed current distribution image is compared to that of the simulation.

Keywords

magnetic source imaging; magnetic field map; current distribution imaging; SERF; OPM; magnetometer

I. Introduction

Magnetic source imaging refers to reconstructing the magnetic and current dipoles underlying measured magnetic field maps. Magnetic source imaging has a wide range of applications such as magnetoencephalography (MEG) [1–5], magnetocardiography (MCG) [6–9], material science [10–12], printed-circuit-board/integrated-circuits quality-assurance [13–15], magnetic nanoparticle detection [16], etc. The type of magnetic sensor and its underlying sensing mechanism dictates various system level specifications including noise, dynamic range, and bandwidth. In [15] a superconductive quantum interference device (SQUID) magnetometer is used to detect faulty integrated circuits (IC); due to the small area of integrated circuits, a high spatial resolution system is required; hence a single-channel SQUID with a pick-up coil area of 10^{-4} mm2 is indexed over the powered-up IC to capture its magnetic field map. For imaging applications, where high sensitivity is not critical, giant magnetoresistive (GMR) sensors [17], Hall-effect sensors [10, 11], or fluxgates sensors [18] can also be used for magnetic field sensing. Magnetic Imaging systems implemented using GMR benefit from high spatiotemporal resolution inherent in GMR sensors; however, poor noise performance of GMR sensors, ~0.2 $nT/\sqrt{Hz}$, prevents their usage in imaging small magnetic fields, e.g. MEG.

Optically pumped magnetometers (OPMs) can be configured in a wide variety of ways for different MSI applications. Recently optically pumped magnetometers (OPM) operating in the spin-exchange-relaxation-free (SERF) regime have shown sub-fT sensitivity [19], and been used to localizes neuronal current sources within the human brain [20, 21]. By combining highly sensitive SERF OPM sensors with flux-guides, an indexed, high resolution magnetic field imaging system is demonstrated in [22, 23]. Another modality of magnetic source imaging is magnetic induction tomography (MIT) [24–26]; in MIT, the electromagnetic fields, emanating from the induced eddy currents in conductive objects, are detected. In [25, 26], by using a Rb alkali-vapor cell magnetometer, sub-mm features in conductive objects are resolved. In [27], a magnetic source imaging camera is developed by using charge-coupled device (CCD) camera; in this system, the sensed magnetic field is encoded in the fluorescence light from the Cs atoms of a vapor cell exposed to the magnetic field; each camera pixel acts as a magnetometer channel, yielding a magnetic imaging system with high spatial resolution.

We have developed a 4-channel SERF OPM sensor [28], shown in Fig. 1, and have successfully employed this sensor in an array configured for magnetoencephalography [29]. However, despite the high sensitivity of SERF OPMs, due to near zero magnetic field operation, the dynamic range of these sensors is limited. In this paper, we expand the upper sensing range of our OPM sensors by operating them in pulsed-mode as described in Section II.A; Section II.B presents the hardware of the magnetic field-mapping system featuring six pulsed-OPM sensors. Signal processing techniques used for source imaging is described in Sections II.C-D. Section III presents simulation and experimental results, and Section IV is the conclusion of the manuscript.

II. Materials and Methods

A. The Sensor: Pulsed Optically Pumped Magnetometer

The basic optical layout and the construction of the our OPM is described in [28], and we briefly describe it here. In each 4-channel sensor module (Fig. 1), four laser beams propagate through a glass cell filled with ^{87}Rb vapor and 600 Torr of N_2, and the volume illuminated by a particular beam within the vapor cell determines the location of the magnetic field measurement for the particular channel. Light enters the magnetometer via a polarization maintaining optical fiber carrying both the pump laser, tuned to the D1 transition of ^{87}Rb at 795 nm, and the probe laser, tuned to the D2 transition at 780 nm. The light is split into four beams by a diffractive optical element, traverses the vapor cell, and is reflected back to the detection optics. In the detection optics, the pump beam is rejected, and the angle of the polarization of the probe beam, for each individual channel, is measured with a balanced polarimeter.

OPM sensors operating in the SERF regime yield the highest sensitivity [19] amongst atomic magnetic sensors, a quality highly desirable for magnetic imaging systems. While our sensor was designed as a SERF magnetometer, the present application requires the measurement of magnetic fields on the order of hundreds of nT, a magnitude beyond the dynamic range of our SERF magnetometers. Larger fields are typically measured with OPMs by using a scalar magnetometer technique, e.g. an M_x [30] or Bell-Bloom [31, 32]

configuration. However, for our array these configurations are not appropriate due to the large gradients across the array (~ 400 nT in the applied bias field). The large magnetic field gradient across the array leads to a varying Larmor precession frequency across channels and sensors. In the M_x configuration, an oscillating magnetic field is applied to the atoms at their Larmor precession frequency. However, each channel in our array would require a different frequency, and there would be significant interference between neighboring sensors. In the Bell-Bloom magnetometer, the pump laser is modulated at the Larmor precession frequency. However, for our application, the large gradients would require a different modulation frequency for each channel within a given sensor, which is not possible with our sensor design.

To accommodate the limitations imposed by the array geometry and the large gradient, we have developed a pulsed-mode technique for the OPM that makes a scalar measurement of the magnitude of the total magnetic field (a similar technique is shown in [33]). The pulsed-mode operation is schematically shown in Fig. 2 and is comprised of two phases, a polarization phase and a sensing phase. During the polarization phase, a magnetic field ($\overrightarrow{B_{POL}}$) is applied parallel to the propagation axis of the pulsed, circularly polarized pump laser. The pump laser optically pumps the atomic spins parallel to the propagation axis. $\overrightarrow{B_{POL}}$ is generated by on-sensor coils printed on a flexible circuit board and wrapped around the outside of each 4-channel sensor and is approximately 840 nT. A larger amplitude field would enhance the atomic polarization. While more current and coil turns would increase $\overrightarrow{B_{POL}}$, a redesign of the on-sensor coils and the coil driver was not necessary for this experiment. The polarization field magnitude of 840 nT was large enough that it was not the dominating error source of the total measurement error. In the sensing phase, both the pump laser and $\overrightarrow{B_{POL}}$ are turned off, and a large bias field ($\vec{B}_0$) is applied, around which the atoms precess. Unlike the polarization field $\overrightarrow{B_{POL}}$), the bias field ($\vec{B}_0$) is generated using large coils embedded in the magnetic shield. The probe laser is not modulated; hence the channels can be sensed during both phases, as shown in Fig. 3. The frequency of the decaying sinusoid, shown in the sensing phase of Fig. 3, is the Larmor precession frequency of the atoms and is converted into the magnitude of the sensed magnetic flux density using the gyromagnetic ratio of the ^{87}Rb atoms.

B. The Magnetic Sensing System

The 24-channel OPM array is housed inside a three-layer μ-metal cylindrical shield, whose inner shield has a diameter of 1 m. The complete magnetic sensing system [29], shown in Fig. 4, is composed of: 1) the six OPM sensors [28], 2) a 3D printed sensor holder, 3) magnetic shield, 4) a temperature control board, 5) a transimpedance amplifier board, 5) data acquisition hardware, 6) a signal conditioning board, 7) the laser system, and 8) shield coils that apply $\vec{B}_0$ (~ 1 μT) longitudinally to the cylindrical magnetic shield. The fibers, cables and tubes, seen to the left of the array, provide the lasers (795 nm and 780 nm), heating current (~ 250 mA @ 33 V_{pp}), and airflow to cool the sensors, and conduct the current signals of the sensors' differential photo diodes out of the array.

The laser system is composed of two distributed feedback laser diode sources: a pump laser which is tuned to the rubidium D1 line, and a probe laser which is tuned to 133 GHz from the rubidium D2 line. Both lasers are amplified by tapered amplifiers. The laser system is similar to the one implemented in [29] with a few modifications: 1) the pump-laser is monochromatic, 2) the pump-laser is switched with an acousto-optic modulator, and 3) the power of both pump and probe lasers are *not* actively controlled. The temperature controller board heats up the vapor cells, within 1 °C variation, to −120 °C.

A digital-to-analog converter provides signals to control the pulsing of the polarization coils, the shield coils that provide the bias field, and the pump laser. The transimpedance amplifier (TIA) board, contains circuitry to amplify the 24 current signals from the differential in-sensor photo-diodes. The data acquisition system is composed of analog-to-digital converters (ADC) with a 100 kS/s conversion rate and 24-bit resolution. The amplified photodiode signals along with the laser-modulating signal are digitized and are post-processed to determine the magnetic field.

C. Signal Processing Techniques: Extracting the Magnetic Field

Each sensing phase, shown in Fig. 3, yields a single data point reflecting the frequency of the exponentially decaying sinusoid. The extracted frequency is converted into magnitude of the sensed magnetic flux density (|B|) using the gyromagnetic ratio (γ) of the rubidium (^{87}Rb) atoms (7 Hz/nT). The signal of the decay of the atomic polarization in the sensing phase can be expressed as [34]:

$$f(t) = A_1 e^{-t/T_1} + A_2 e^{-t/T_2} \cos\left(2\pi f_0 t + \varphi_0\right) + n(t) \quad (1)$$

In (1), $n(t)$ is the noise; A_1 is the amplitude of the longitudinal polarization; A_2 is the amplitude of the trans-verse polarization; T_1 and T_2 are longitudinal and tangential relaxation times, respectively; φ_0 is the phase of the decaying sinusoid; and finally, f_0 is the Larmor precession frequency which is to be extracted.

To extract the frequency, first the raw signal (Fig. 3) is bandpass filtered from 1 kHz to 20 kHz, using a two-pass, 4th order Butterworth filter. It should be noted that the magnitude of the sensed magnetic field is contained in the decaying sinusoid's frequency during the sensing phase and will be preserved by the band pass filtering procedure. Next, all zero crossings of the signal's first derivative are fitted with a third-order polynomial. The roots of the fitted polynomials will be used to calculate the frequency of the signal. The fitting procedure is necessary to avoid discontinuities in the extracted frequency which are a direct result of the small ratio of the raw signal's limited sampling frequency (100 kS/s) to the decaying sinusoid's frequency (~ 10 kHz). Working with the first derivative's zero crossings rather than those of the main signal improves the output stability as the low frequency drifts introduced by the first exponential term in (1) will be reduced by the derivative operation.

The large bias magnetic field is set to ~1 μT, and assuming it is much larger than the magnetic field contributed by the device under test ($\left|\overrightarrow{B_0}\right| \gg \left|\overrightarrow{B_{DUT}}\right|$), the extracted magnetic field can be expressed as:

$$\left|\overrightarrow{B_{OPM}}\right| = \sqrt{\left|\overrightarrow{B_{DUT,x}}\right|^2 + \left|\overrightarrow{B_{DUT,y}} + \overrightarrow{B_{0,y}}\right|^2 + \left|\overrightarrow{B_{DUT,z}}\right|^2} \approx \sqrt{\left|\overrightarrow{B_{DUT,y}} + \overrightarrow{B_{0,y}}\right|^2} = \left|\overrightarrow{B_{DUT,y}} + \overrightarrow{B_{0,y}}\right| \quad (2)$$

In (2), it is assumed that the bias field ($\overrightarrow{B_0}$) is aligned with the y-axis. If the bias field is aligned with an axis other than the Cartesian orthonormal basis, the magnitude of the magnetic field measured by the pulsed OPM can be interpreted as a vector measurement along the bias field axis. The validity of (2), depends on the ratio of $\left|\overrightarrow{B_{DUT}}\right| / \left|\overrightarrow{B_0}\right|$ and the angle between $\overrightarrow{B_0}$ and $\overrightarrow{B_{DUT}}$. The largest error is when the sensed magnetic field, $\overrightarrow{B_{DUT}}$, is orthogonal to the bias field. A calculation of the error reveals that for a bias field $\overrightarrow{B_0}$ of 1 μT and a sensed magnetic field $\left|\overrightarrow{B_{DUT}}\right|$ of 200 nT, (2) is valid to within 10 % as shown in Fig. 5.

The data rate of the overall imaging system is dictated by the pump laser's modulation frequency. The higher the data rate, the higher the bandwidth of the signal path; however, there are tradeoffs between signal-to-noise ratio (SNR), bandwidth, and dynamic range. To minimize the calculation error in extracting the frequency of the atomic polarization's decay signal in the sensing phase, f_0 in (1), the ratio of the ADC's sampling frequency to the extracted frequency should be large. On the other hand, the higher the bias field, the more accurate the approximation in (2); considering, the sampling frequency of the employed analog-to-digital converter (100 kS/s) we have selected a bias field ($\left|\overrightarrow{B_0}\right|$) of 1 μT which results in an f_0 of 7 kHz ($\gamma \times \left|\overrightarrow{B_0}\right|$). Furthermore, to have (2) valid, the maximum magnetic field contribution by the device under test (DUT) should be a small percentage of the bias field as shown in Fig. 5. Currently the data rate of the magnetic sensing system is set to 500 S/s.

D. Current Distribution Imaging: The Inverse Problem

The goal of the inverse problem is to construct the underlying current density distributions from the measured magnetic field. There is no unique solution to the inverse problem, however its solution can be greatly simplified assuming a 2D current density distribution. The mathematical algorithm introduced in [35] is implemented for 2D imaging of the underlying current density distribution. There are four main assumptions facilitating solving the inverse problem: 1) the current density distributions are two-dimensional, 2) Maxwell's equations can be approximated in quasistatic regime, and 3) the current is quasistatic ($\partial\rho/\partial t + \nabla \cdot \mathbf{J} = \nabla \cdot \mathbf{J} = 0$). From the Biot-Savart law [36], and assuming a 2D current density distribution, the magnetic field can be derived as [35]:

$$B_y(x,y,z_0) = \frac{\mu_0 d}{4\pi} z_0 \int_{-\infty}^{+\infty}\int_{-\infty}^{+\infty} \frac{J_x(x',y')}{\left[(x-x')^2+(y-y')^2+z_0^2\right]^{\frac{3}{2}}} dx'dy' \quad (3)$$

In (3), it is assumed that the current carrying structure is on the xy-plane with $z = 0$; the sensors are laid out on a 2D plane parallel to the xy-plane with $z = z_0$; d is the thickness of the traces conducting current; z_0 is the distance between the measurement plane and the sensor plane; $B_y(x, y)$ is the y-axis component of the magnetic field sensed at the sensor's cartesian coordinates (x, y, z_0); and $J_x(x', y')$ is the current density's x-component. (3) can be interpreted as the convolution of the current density's x-component with a Green's function defined as [35]:

$$G(x,y,z_0) = \frac{\mu_0 d}{4\pi} z_0 \frac{1}{\left[x^2+y^2+z_0^2\right]^{\frac{3}{2}}} \quad (4)$$

$$FT2D\{G(x,y,z_0)\} = \left(\frac{\mu_0 d}{2}\right)\exp\left(-z_0\sqrt{k_x^2+k_y^2}\right) \quad (5)$$

In above equations, k_x and k_y are spatial frequency components of the x and y-axis, respectively; and $FT2D$ is the two-dimensional Fourier transform [37]. By taking the two-dimensional Fourier transform of the quasistatic current equation ($\nabla \cdot \mathbf{J} = 0$), both components of the current density can be calculated from the measured y-component of the magnetic field as [35]:

$$J_y(x,y) = FT2D^{-1}\left\{-\frac{k_x}{k_y}\frac{FT2D\{B_y(x,y,z_0)\}}{FT2D\{G(x,y,z_0)\}}\right\} \quad (6)$$

$$J_x(x,y) = FT2D^{-1}\left\{\frac{FT2D\{B_y(x,y,z_0)\}}{FT2D\{G(x,y,z_0)\}}\right\} \quad (7)$$

In above equations, $FT2D^{-1}$ refers to inverse two-dimensional Fourier transform [37]. As shown in previous section, the presented pulsed OPM array measures the magnetic field vector along the bias field (2). Hence if the bias field is aligned with the y-axis, the array output will be $B_y(x, y, z_0)$, and the current density distribution of the DUT located below the sensor plane can be calculated using (6) and (7).

III. Results and Discussion

A. Test Setup

To evaluate the functionality of our magnetic imaging system, we measured a planar coil structure (Fig. 6) carrying DC current with the magnetometer array; the magnetic field map and the current density image of this structure was simulated and the results were compared to that of the measurement. The two coils are fabricated on a flexible PCB using pure copper and fixed to a plastic plane. The plane of the two coils is positioned 2.8 cm away from and parallel to the sensor plane. The two coils are driven by the DAC controlled via the host computer. A sequence of DC current signals (19 mA) is applied to the coils. The time-domain magnetic field measured by one of the channels is shown in Fig. 7. To create a synthetic array, the device under test (the plane containing the two coils) is indexed for a total of 8 times with a spacing of 36 mm along the array's y-axis (Fig. 8). Therefore, the total number of the synthetic array channels is 192.

B. Baseline Characterizing

As stated in Section II.C, to have (2) valid, the following inequality must hold true $\left|\overrightarrow{B}_0\right| \gg \left|\overrightarrow{B_{DUT}}\right|$. Furthermore, the larger the number of the decaying sinusoid's zero crossings (Fig. 3), the lower the noise floor of the extracted frequency. Hence, there will be a tradeoff between noise floor, data rate, and dynamic range. In the presented pulsed-OPM array the bias field magnitude is set to ~1 μT and pulsed at 500 Hz (f_s) with 50% duty cycle; the bandwidth of the overall signal path is $f_s/2 = 250 Hz$. The bias field is generated by driving two large coils providing a field longitudinal to the cylindrical shield. To determine which component of the magnetic field of the device under test is predominantly measured, the direction of the bias field must be known. This is measured with a commercial fluxgate magnetometer. Ideally the generated bias field is homogenous and aligned with the longitudinal axis. However, because the array is neither centered in the shield nor centered between the two coils, the bias field has a ~25° angle with the y-axis (longitudinal axis). The vector field map of the bias field measured using a commercial fluxgate is shown in Fig. 8-a; this measurement agrees well with the bias field's magnitude measurement by the pulsed-OPM array shown in Fig. 8-b. There is a 400 nT gradient across the array. The noise spectrum of the best magnetometer channel is shown in Fig. 9-a, with a noise floor of ~0.8 $pT/\sqrt{Hz}$. The histogram of the array channels noise floor is shown in Fig. 9-b. Through measurement, it is verified that the main noise contributor is the bias magnetic field generator circuitry; however other system components such as the probe laser light, in-sensor photo diodes, the ADC system, and photon shot noise contribute to the overall system noise as well. Furthermore, since the inequality $\left|\overrightarrow{B_0}\right| \gg \left|\overrightarrow{B_n}\right|$ holds true for noise, the component of the measured noise along the y-axis will be added linearly to the measured signal according to:

$$\left|\overrightarrow{B_{OPM}}\right| = \left|\overrightarrow{B_{DUT,y}} + \overrightarrow{B_{0,y}} + \overrightarrow{B_{n,y}}\right| \quad (8)$$

To have (2) valid with an error of less than 3%, $\left|\overrightarrow{B_{DUT,max}}\right| < \left|\overrightarrow{B_0}\right|/20$; hence, with a 1 μT bias field, the maximum signal sensed by the array is 50 nT, resulting in a dynamic range of 72 dB.

C. Capturing Magnetic Signature

Using the Biot-Savart law [36], the magnetic field generated by the coils for single and double-coil configurations is simulated and used as a baseline comparison against the results measured by the pulsed-OPM array. To that aim, the coils (Fig. 6) were implemented as thin wires (5-mil thickness). The magnetic field is simulated on a plane 2.8 cm away from and parallel to the plane of the two coils. As shown in Fig. 8, the measured bias field generated by the two large longitudinal coils has a 25 ° angle with the y-axis; in simulation, a bias field with the same profile as the measured one is added to the simulated magnetic field from the coils. Finally, we subtract the magnitude of the simulated bias field from the magnitude of the total simulated magnetic field to extract the magnetic field from the coils (Figs. 10 and 11). Assuming the validity of the inequality, $\left|\overrightarrow{B_{0,\ sim}}\right| \gg \left|\overrightarrow{B_{DUT,\ sim}}\right|$, the component of the simulated magnetic field from the coils parallel to the simulated bias field ($\overrightarrow{B_{0,\ sim}}$) is extracted.

For the OPM measurements, the coils are indexed across the array as explained in III.A and for each index the entire time-domain waveform, shown in Fig. 7, is applied to the coils. The field maps of the 192 channels of the synthetic array along with that of the simulated results are plotted using FieldTrip [38]. The results for the case where only a single coil is energized with 19 mA of DC current, are shown in Fig. 10. It should be noted that the resolution of the measurement (192 grid-points) is lower than that of the simulation (256×225 grid-points), however the interpolation algorithm embedded in FieldTrip [38], enhances the field map quality of the measured results. Fig. 11 depicts the results for the case where both coils are energized using 19 mA of DC current. From the field maps, the magnetic fields generated by two coils are similar to the energized single-coil field map in terms of magnitude and polarity. The minor differences between the measured and simulated field maps (Fig. 10–11) is most likely due to drifts in the current generating $\overrightarrow{B_0}$, while other factors include a difference in grid points.

D. Imaging 2D Magnetic Sources

An example application of the pulsed-OPM system is measuring the magnetic field of a system of interest and then calculating the underlying current distribution. This problem is regarded as the *inverse problem* and in general does not possess a unique solution [1]. There is strong interest in MEG and MCG communities to solve the inverse problem and calculate the current sources responsible for the observed biomagnetic signals. Among the available methods, equivalent current dipole (ECD) [1, 4] and beamforming [1–3] algorithms are widely used in MEG applications. Furthermore, current distribution imaging to detect faulty integrated circuits (IC) and printed circuit boards (PCB) has been in use since the early 80s [13–15]; in most of these approaches, the sensor of choice has been the superconductive quantum interference device [39]. In this paper, we have implemented the method

introduced in [35] and outlined in Section II.D, for imaging the magnetic sources using the field maps captured by our pulsed-OPM array. Assuming a 2D current distribution, the inverse problem can be uniquely solved using (6) and (7).

For validation, the same 2D imaging algorithm is implemented on the simulated field map of a single test coil device shown in Fig. 10. If the large bias field is tilted by α with respect to the y-axis, the simulated field map is rotated by$-\alpha$ as the first step in the current density reconstruction; this step aligns the bias field with the y-axis, so (6) and (7) can be applied to the field map data. From (2) we assume that the simulated magnitude of the rotated field map stems from the y-axis component of the magnetic field ($|\overrightarrow{B}_y|$). In the next step, assuming a thickness of 125 μm *(d)* and a sensor plane-to-coil-plane distance of 2.8 cm (z_0) the two-dimensional Fourier transform of the Green function, i.e. (5), is calculated. Applying (6) and (7) to the two-dimensional Fourier transform of the simulated magnetic field ($|\overrightarrow{B}_y|$) allows the 2D current densities to be uniquely calculated. The same method is applied to the measured pulsed-OPM data and the results of the 2D current density imaging are shown in Fig. 12. For the simulated current density image, the exact location of the coil is known and superimposed on the estimated current density (Fig. 12-a). For the measured field maps (Fig. 12-b) the location of the coil is estimated measuring with a ruler the position of the coil relative to the array.

E. Discussion

The precision of the reconstructed current density image (J_y and J_x) depends on the following factors: 1) the sensors' SNR, 2) spatial resolution of the array, i.e. sensor spacing, and 3) the distance (z_0) between the sensors and DUT. The reconstructed current distribution image from the field maps measured by the pulsed-OPM system (Fig. 12-b) captures the four sides of the rectangular coil structure and is very similar to the current density image reconstructed from the simulated data (Fig. 12-b). Increasing the sensor density and reducing the measurement gap (z_0) improves the spatial resolution of the system. By inspecting (4)-(7) it can be concluded that the current density image is a high pass filter of the Fourier transform of the magnetic field map [35]; due to the high pass filtering effect it is essential to remove the high spatial frequency noise components of the magnetic field map. Therefore, the system's spatial resolution, sensors noise performance, and the measurement gap (z_0) are all interrelated and should be co-optimized according to the target structure.

The array's SNR depends on the measurement distance (z_0), the current density of the device under test, sensors noise performance, and the measurement time. For DC measurements and imaging, e.g. the ones presented in this work, measurement time can be increased arbitrarily until the noise ($\frac{N_s}{\sqrt{f_s \times T}}$) drops down to well below the magnetic field from the device under test; f_s is the array's data rate and set to 500 S/s, T is the measurement time and N_s is the noise density of the sensors white noise. Fig. 13 shows the dependency of the constructed current density image quality on the measurement gap (z_0) and array's spatial resolution or sensor spacing. In this figure a 1-cm wide square trace with a side of 30 cm (L) and carrying 19 mA of current is constructed for varying measurement distance and

sensor spacing; Fig. 13-a shows the 2-dimensional correlation between the current carrying trace and the constructed current density image; Fig. 13-b shows the current carrying trace against which the constructed current density image is correlated; Fig. 13-c shows the constructed current density image for a 70 % correlation and Fig. 13-d depicts that of the 25 % correlation. In Fig. 13-a, the measurement gap (z_0) is swept from 1.5 % to 160 % of the square's side length (L), and the sensor spacing varies from 1.5 % to 16 % of the square's side length (L). We define an arbitrary cutoff point as 25 % correlation beyond which the constructed current density image does not resemble the original current carrying trace; the contour of 25 % correlation is labeled on Fig. 13-a. For measurement gap/distance (z_0) up to $\boldsymbol{L}/3$ the quality of the constructed current density image improves with higher sensor density; however, for measurement gaps beyond $\boldsymbol{L}/3$ this dependency is diminished.

By inspecting the constructed current density image (Fig. 12), it could be concluded that the increased normalized current densities seen along the short sides of the rectangular structure, stem from the magnetic field contribution of the small inner rectangles; however, when rotating the large bias field by 90 °, the reconstructed current density image shows increased current level for the long edges. To operate the synthetic pulsed-OPM array we employ a large bias field, as stated in Section II.C, and the wires more perpendicular to the bias field will be assigned a higher weight by the imaging algorithm.

IV. Conclusions

We have developed a pulsed optically pumped magnetometer array for magnetic sensing and current imaging applications. The pulsed-OPM system has a noise floor of 0.8 $pT/\sqrt{Hz}$, a sampling frequency of 500 S/s (bandwidth ~250 Hz), and a dynamic range of 72 dB. By comparing the experimental results to the simulation results, we have shown the robustness of our system in capturing the magnetic signature of a general planar 2D coil structure. And finally, we have successfully reconstructed an image of the planar 2D coil's current density using the magnetic field map measured by the pulsed-oPM system. The choice of sensor for a magnetic imaging system depends on several factors outlined in Table I. If high sensitivity is not required, then the fluxgate, giant magneto resistive (GMR), and Hall effect sensors are a good choice. For applications needing higher sensitivity, OPMs and SQUID sensors are required. While SQUIDs are very sensitive, their requirement for cryogenic cooling and expense may rule them out. For OPMs, the SERF magnetometer is excellent for biomagnetic imaging but may not have the dynamic range needed for other applications, The M_x OPM is likely not a good choice for forming an array because neighboring sensors may interfere with each other due to the applied oscillatory magnetic field in each sensor. The Bell-Bloom OPM has no between-sensor interference and is an equally good choice as the pulsed OPM presented in this work as long as the laser light modulation frequency in each Bell-Bloom OPM can be selected independently. Our next step, is to demonstrate our array and the 2D FFT-based current imaging technique outside the magnetic shield.

Acknowledgement

Sandia National Laboratories is a multimission laboratory managed and operated by National Technology and Engineering Solutions of Sandia, LLC, a wholly owned subsidiary of Honeywell International, Inc., for the U.S. Department of Energy's National Nuclear Security Administration under contract DE-NA0003525. This work was

supported by the Office of Defense Nuclear Nonproliferation Research and Development of the National Nuclear Security Administration. The sensor array is developed using Grant Number R01EB013302 from the National Institute of Biomedical Imaging and Bioengineering within the National Institutes of Health.

References

[1]. Hämäläinen M, Hari R, Ilmoniemi RJ, Knuutila J, and Lounasmaa OV, "Magnetoencephalography-theory, instrumentation, and applications to noninvasive studies of the working human brain," Rev. Mod. Phys, vol. 65, no. 2, pp. 413–497, 4 1993.

[2]. Iivanainen J, Stenroos M, and Parkkonen L, "Measuring MEG closer to the brain: Performance of on-scalp sensor arrays," Neuroimage, vol. 147, pp. 542–553, 2017. [PubMed: 28007515]

[3]. Brookes MJet al., "A general linear model for MEG beamformer imaging," Neuroimage,Article vol. 23, no. 3, pp. 936–946, 11 2004. [PubMed: 15528094]

[4]. Lutkenhoner B, "Current dipole localization with an ideal magnetometer system," Ieee Transactions on Biomedical Engineering,Article vol. 43, no. 11, pp. 1049–1061, 11 1996. [PubMed: 9214823]

[5]. Okada Yet al., "BabyMEG: A whole-head pediatric magnetoencephalography system for human brain development research," Rev Sci instrum, vol. 87, no. 9, p. 094301, 9 2016. [PubMed: 27782541]

[6]. Sun WX and Kobayashi K, "Estimation of Magnetocardiography Current Sources Using Reconstructed Magnetic Field Data," ieee Transactions on Magnetics, Article; Proceedings Paper vol. 53, no. 11, p. 4, 11 2017, Art. no. 5100404.

[7]. Alem O.et al., "Fetal magnetocardiography measurements with an array of microfabricated optically pumped magnetometers," Physics in Medicine and Biology,Article vol. 60, no. 12, pp. 4797–4811, 6 2015. [PubMed: 26041047]

[8]. Lembke G, Erne SN, Nowak H, Menhorn B, Pasquarelli A, and Bison G, "Optical multichannel room temperature magnetic field imaging system for clinical application," Biomedical Optics Express, Article vol. 5, no. 3, pp. 876–881, 3 2014. [PubMed: 24688820]

[9]. Bison Get al., "A room temperature 19-channel magnetic field mapping device for cardiac signals," Applied Physics Letters, vol. 95, no. 17, 10 26 2009.

[10]. Xing W, Heinrich B, Zhou H, Fife AA, and Cragg AR, "Magnetic flux mapping, magnetization, and current distributions of $YBa_2Cu_3O_7$ thin films by scanning Hall probe measurements," Journal of Applied Physics, Article vol. 76, no. 7, pp. 4244–4255, 10 1994.

[11]. Herrmann J, Savvides N, and Muller KH, "Nondestructive evaluation of current flow in flat electrical conductors using scanning Hall probe magnetometry," in Nondestructive Characterization of Materials Ix, vol. 497, Green RE, Ed. (AIP Conference Proceedings, Melville: Amer Inst Physics, 1999, pp. 214–219.

[12]. Higashikawa Ket al., "Magnetic Microscopy for Nondestructive Characterization of Local Critical Current Distribution in MgB2 Wires With Magnetic Sheath Materials," Ieee Transactions on Applied Superconductivity, Article vol. 26, no. 3, p. 4, 4 2016, Art. no. 6200804.

[13]. Hofer D, Wiesner T, Zagar BG, and Ieee, "Analyzing 2D Current Distributions by Magnetic Field Measurements," in 2012 Ieee international instrumentation and Measurement Technology Conference(IEEE Instrumentation and Measurement Technology Conference, New York: Ieee, 2012, pp. 2061–2066.

[14]. Holzl PA, Wiesner T, Zagar BG, and Ieee, "Quality Assurance for Wire Connections used in Integrated Circuits via Magnetic Imaging," in 2012 Ieee International Instrumentation and Measurement Technology Conference (IEEE Instrumentation and Measurement Technology Conference, New York: Ieee, 2012, pp. 2051–2056.

[15]. Chatraphorn S, Fleet EF, Wellstood FC, and Knauss LA, "Noise and spatial resolution in SQUID microscopy," Ieee Transactions on Applied Superconductivity, Article; Proceedings Paper vol. 11, no. 1, pp. 234–237, 3 2001.

[16]. Dolgovskiy Vet al., "A magnetic source imaging camera," Applied Physics Letters, vol. 109, no. 2, p. 023505, 2016.

[17]. Holzl PA and Zagar BG, “Deconvolution of High-Resolution Magnetic Field Scans for Improved Current Density Imaging,” Ieee Transactions on Magnetics, Article vol. 50, no. 2, p. 4, 2 2014, Art. no. 7002304.

[18]. Oyama D, Adachi Y, Higuchi M, and Uehara G, “Magnetic Marker Localization System Using a Super-Low-Frequency Signal,” Ieee Transactions on Magnetics, Article; Proceedings Paper vol. 50, no. 11, p. 4, 11 2014, Art. no. 5101604.

[19]. Kominis IK, Kornack TW, Allred JC, and Romalis MV, “A subfemtotesla multichannel atomic magnetometer,” Nature, vol. 422, pp. 596–599, 4 2003. [PubMed: 12686995]

[20]. Kim Ket al., “Multi-channel atomic magnetometer for magnetoencephalography: A configuration study,” NeuroImage, Article vol. 89, pp. 143–151, 4 2014. [PubMed: 24185014]

[21]. Boto Eet al., “Moving magnetoencephalography towards real-world applications with a wearable system,” Nature, Article vol. 555, no. 7698, pp. 657–+, 3 2018. [PubMed: 29562238]

[22]. Kim YJ and Savukov I, “Ultra-sensitive Magnetic Microscopy with an Optically Pumped Magnetometer,” Scientific Reports,Article vol. 6, p. 7, 4 2016, Art. no. 24773. [PubMed: 28442712]

[23]. Kim YJ, Savukov I, Huang JH, and Nath P, “Magnetic microscopic imaging with an optically pumped magnetometer and flux guides,” Applied Physics Letters, Article vol. 110, no. 4, p. 5, 1 2017, Art. no. 043702.

[24]. Griffiths H, “Magnetic induction tomography,” Measurement Science and Technology, Article vol. 12, no. 8, pp. 1126–1131, 8 2001.

[25]. Wickenbrock A, Leefer N, Blanchard JW, and Budker D, “Eddy current imaging with an atomic radio-frequency magnetometer,” Applied Physics Letters, Article vol. 108, no. 18, p. 4, 5 2016, Art. no. 183507.

[26]. Deans C, Marmugi L, Hussain S, and Renzoni F, “Electromagnetic induction imaging with a radio-frequency atomic magnetometer,” Applied Physics Letters, Article vol. 108, no. 10, p. 5, 3 2016, Art. no. 103503.

[27]. Dolgovskiy Vet al., “A magnetic source imaging camera,” Applied Physics Letters, Article vol. 109, no. 2, p. 4, 7 2016, Art. no. 023505.

[28]. Colombo APet al., “Four-channel optically pumped atomic magnetometer for magnetoencephalography,” Optics Express, vol. 24, no. 14, pp. 15403–15416, 2016/07/11 2016. [PubMed: 27410816]

[29]. Borna Aet al., “A 20-channel magnetoencephalography system based on optically pumped magnetometers,” Physics in Medicine and Biology,Article vol. 62, no. 23, pp. 8909–8923, 12 2017. [PubMed: 29035875]

[30]. Groeger S, Bison G, Schenker JL, Wynands R, and Weis A, “A high-sensitivity laser-pumped M-x magnetometer,” European Physical Journal D, vol. 38, no. 2, pp. 239–247, 5 2006.

[31]. Gerginov V, Krzyzewski S, and Knappe S, “Pulsed operation of a miniature scalar optically pumped magnetometer,” Journal of the Optical Society of America B-Optical Physics, Article vol. 34, no. 7, pp. 1429–1434, 7 2017.

[32]. Bell WE and Bloom AL, “Optically Driven Spin Precession,” Physical Review Letters, vol. 6, no. 6, pp. 280–281, 1961.

[33]. Sheng D, Li S, Dural N, and Romalis MV, “Subfemtotesla Scalar Atomic Magnetometry Using Multipass Cells,” Physical Review Letters,Article vol. 110, no. 16, p. 5, 4 2013, Art. no. 160802.

[34]. Hopf FA, Shea RF, and Scully MO, “Theory of optical free-induction decay and 2-photon superradiance,” Physical Review A, Article vol. 7, no. 6, pp. 2105–2110, 1973.

[35]. Roth BJ, Sepulveda NG, and Wikswo JP, “Using a magnetometer to image a two-dimensional current distribution,” Journal of Applied Physics, Article vol. 65, no. 1, pp. 361–372, 1 1989.

[36]. R. B. L. Richard P. Feynman, Matthew Sands, The Feynman Lectures on Physics. United States: Addison-Wesley, 1964.

[37]. A. S. W. Alan V. Oppenheim, S. Hamid, Signals and Systems (2nd Edition). United States: Pearson 1996.

[38]. Oostenveld R, Fries P, Maris E, and Schoffelen J-M, “FieldTrip: Open Source Software for Advanced Analysis of MEG, EEG, and Invasive Electrophysiological Data,” Computational Intelligence and Neuroscience, vol. 2011, p. 9, 2011.

[39]. Kirtley JRet al., Advanced sensors for scanning SQUID microscopy (2013 Ieee 14th International Superconductive Electronics Conference). New York: Ieee, 2013.

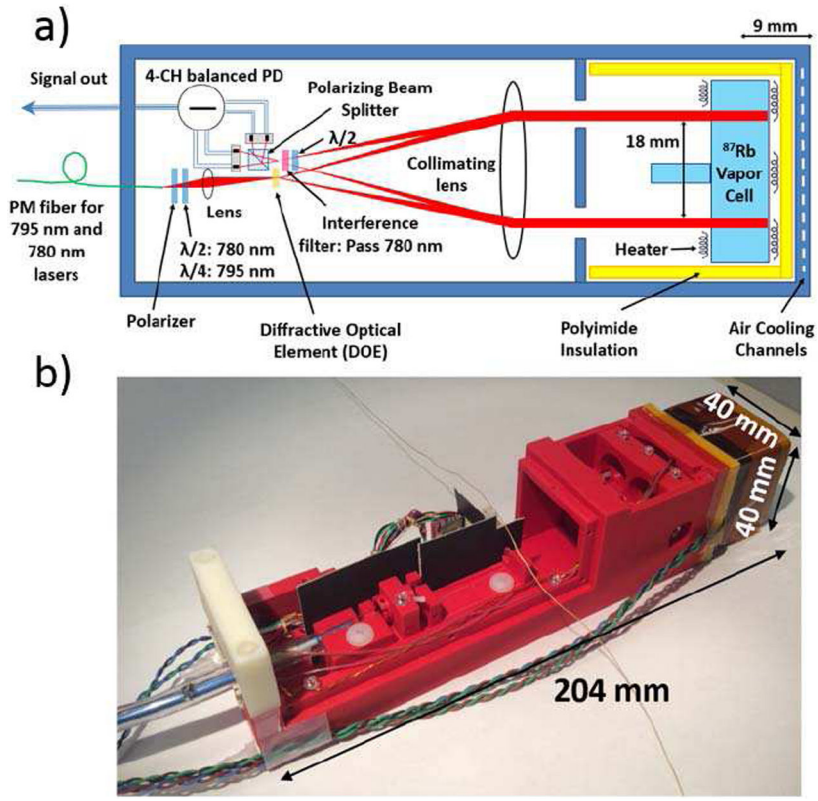

Fig. 1.

Sensor block diagram (a) and photo (b) [28]. PBS: polarizing beam splitter; PM: polarization maintaining, PD: photodiode, $\lambda/2$: half wave plate, $\lambda/4$: quarter wave plate.

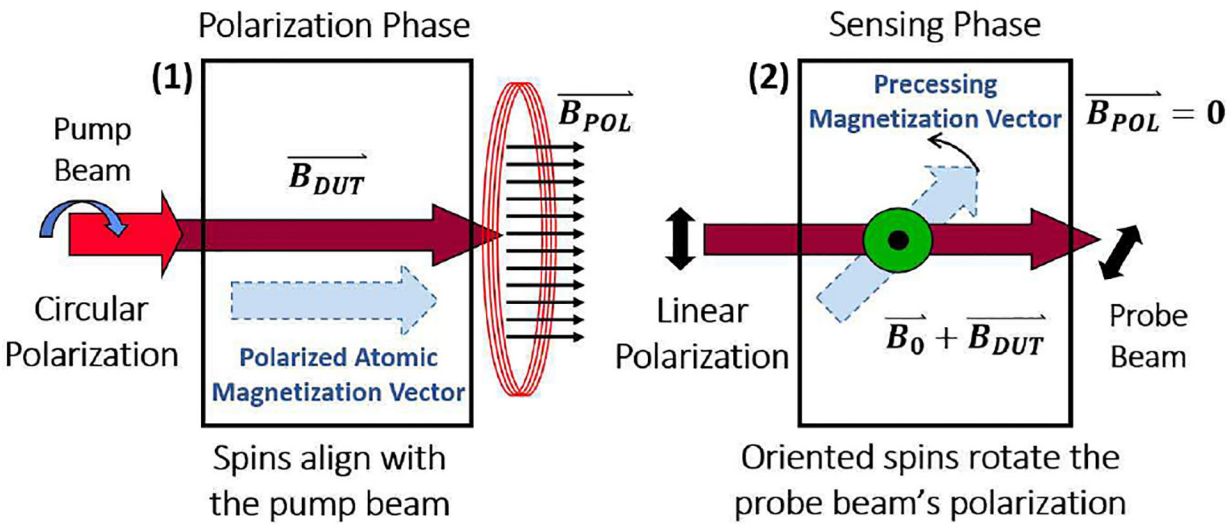

Fig. 2.

Fundamentals of the pulsed optically pumped magnetometers: (1) polarization phase, and (2) sensing phase. The black box represents the vapor cell containing alkali atoms (^{87}Rb). The green circle and black dot in (2) indicate that the bias field $\overrightarrow{B_0}$ is oriented perpendicular to the plane of the drawing.

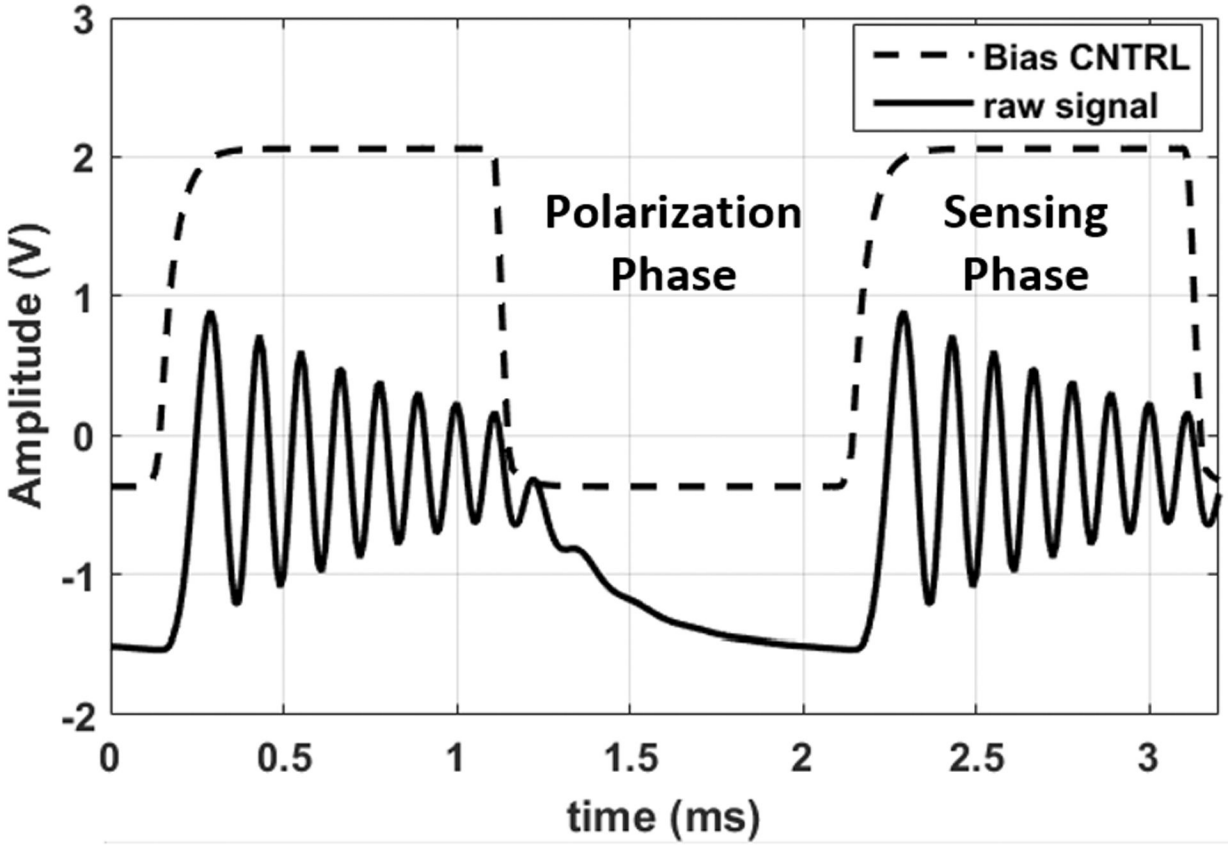

Fig. 3.

The raw waveform of a single channel (solid line), and the control signal for the bias field, $\overrightarrow{B_0}$ (dashed line); the magnitude of the magnetic field during the sensing phase is proportional to the frequency of the decaying sinusoid.

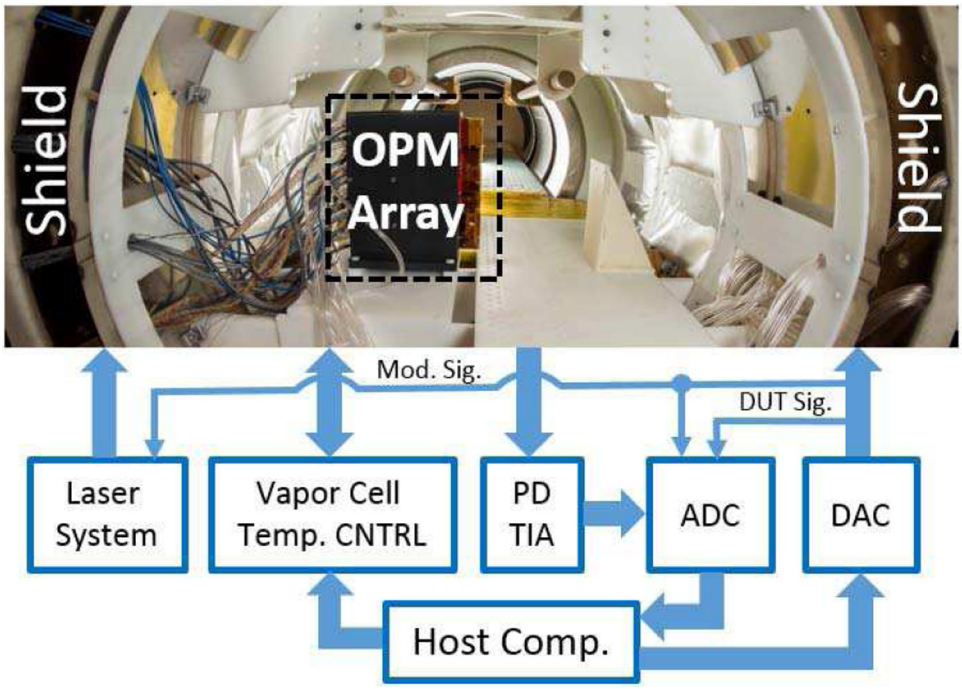

Fig. 4.

The magnetic sensor array inside the three-layer magnetic shield. PD TIA: transimpedance amplifiers of the photo diodes; ADC: analog-to-digital-converter; DAC: digital-to-analog-converter; device under test (DUT) Sig.: the signal driving the device under test; Mod. Sig.: the control signal modulating the laser system, the bias field, and the polarizing magnetic field.

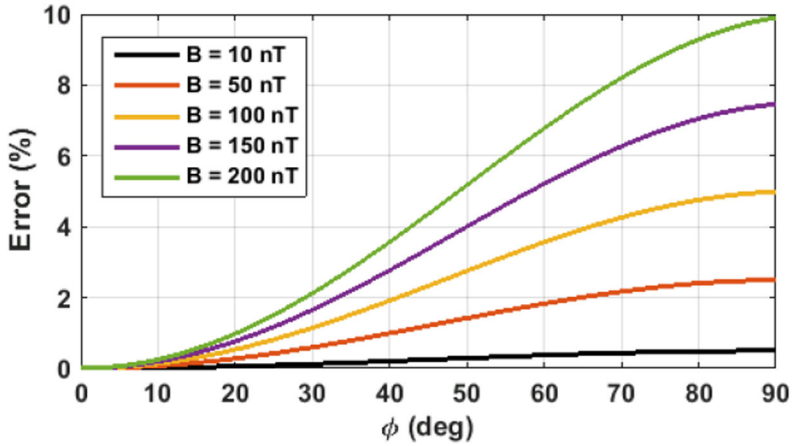

Fig. 5.

Calculated error of the pulsed-OPM magnetic imaging system; the bias field is 1 μT; ϕ is the angle between the sensed magnetic field ($\overrightarrow{B_{DUT}}$) and the bias field ($\overrightarrow{B_0}$). The error is the difference between the magnetic field from the device under test and the magnetic field calculated from the OPM measurements.

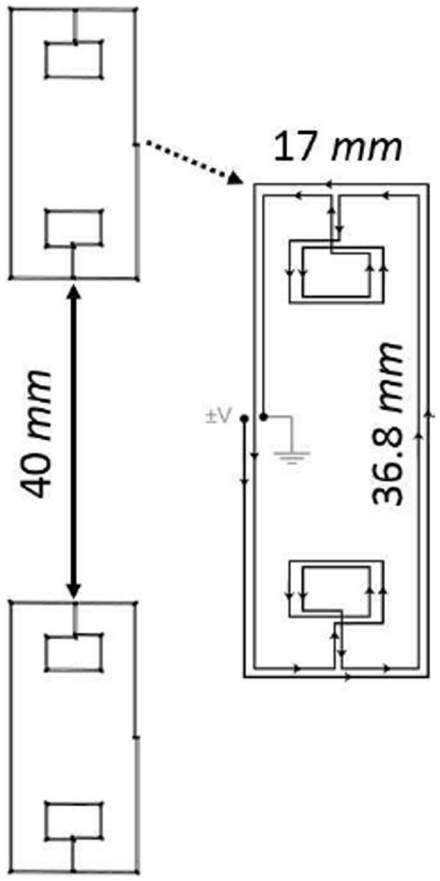

Fig. 6.
Device under test (DUT) coil structure (not to scale).

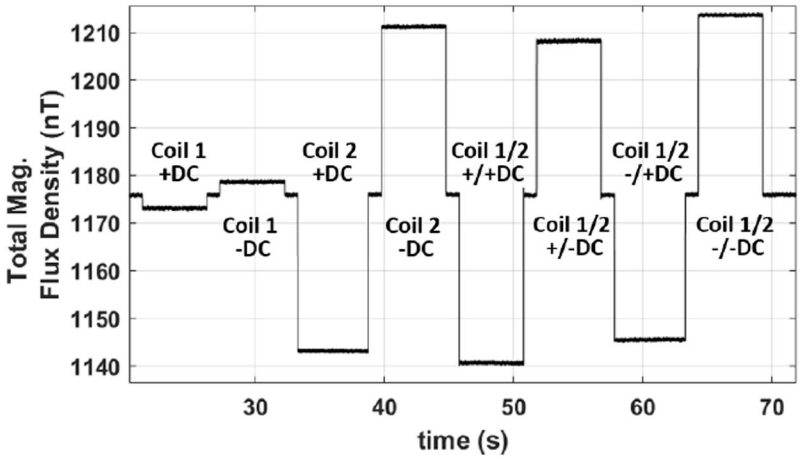

Fig. 7.

Time domain waveform of a measured pulsed-OPM channel when current is applied to the coils in the test structure described in Figure 6.

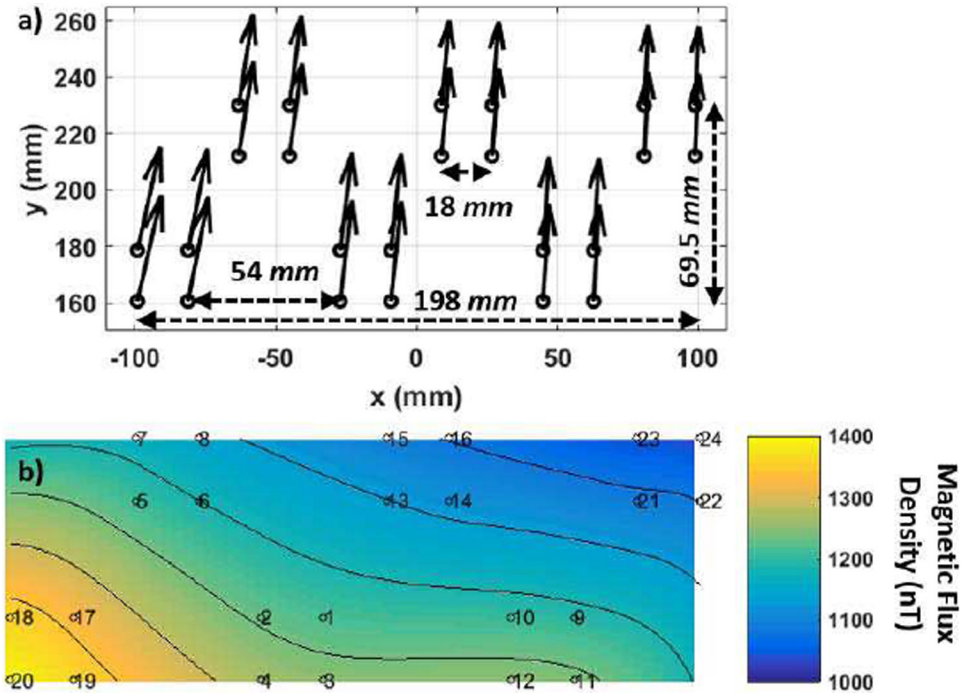

Fig. 8.

The vector field map of the bias magnetic field measured by a commercial fluxgate magnetometer (a), and the bias magnetic field's magnitude measured by the presented OPM array (b). The array's dimensions are indicated on the fluxgate vector field map (a).

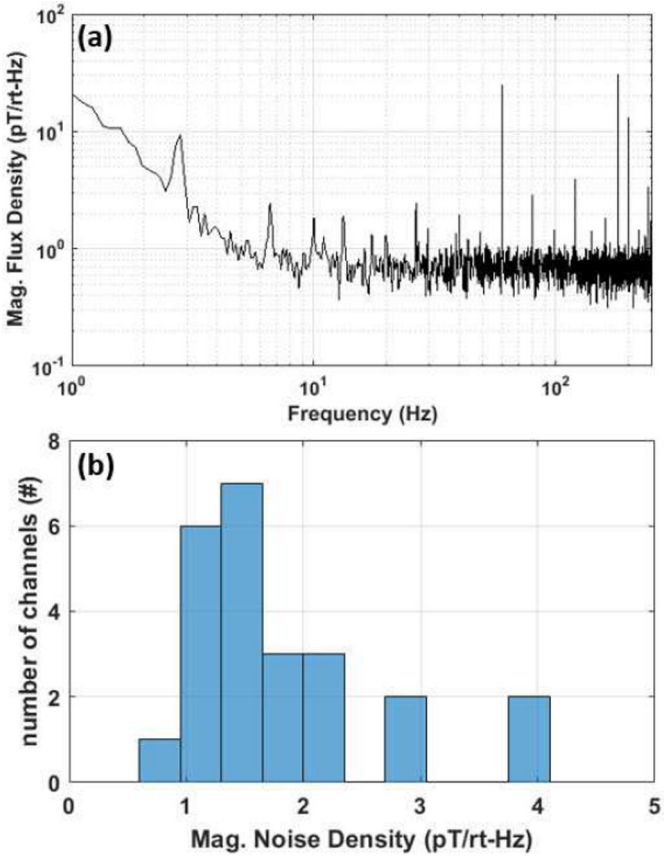

Fig. 9.

The noise spectrum of the pulsed OPM sensor (a) and the 24-channel array noise floor histogram (b).

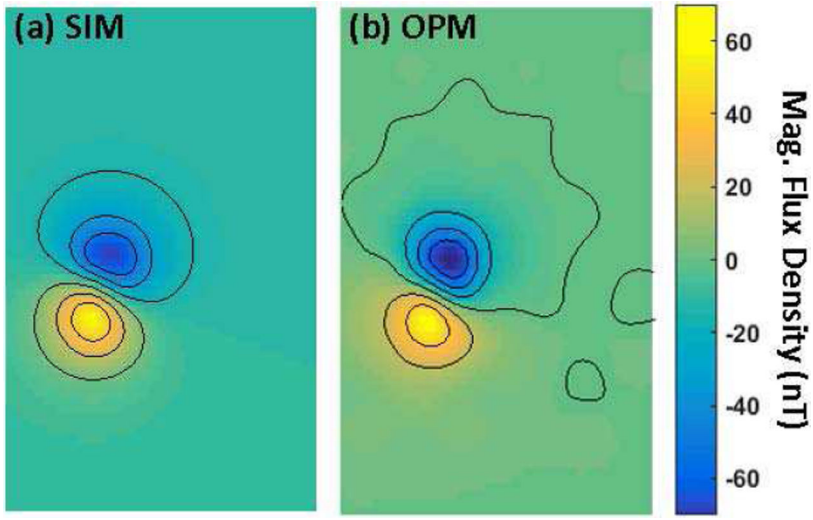

Fig. 10.

Single Coil DC field map simulation (a), and the measured field map using the pulsed-OPM array (b).

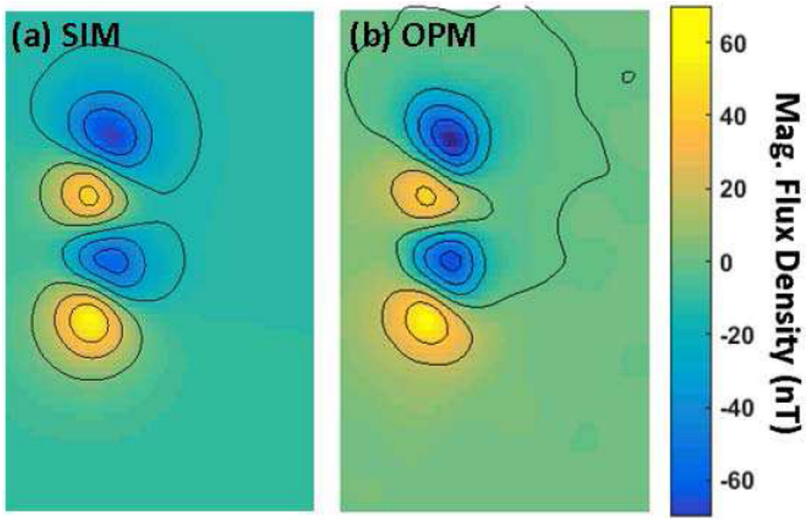

Fig. 11.

Double Coil DC field map simulation (a), and the measured field map using the pulsed-OPM array (b).

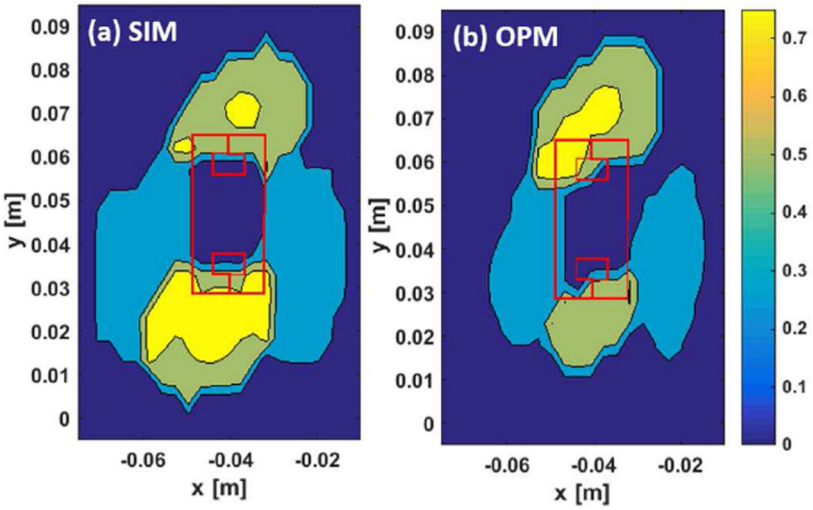

Fig. 12.

Current distribution imaging using simulated (a) and measured (b) magnetic fields. The coil structure is overlaid on top of the constructed current density vectors.

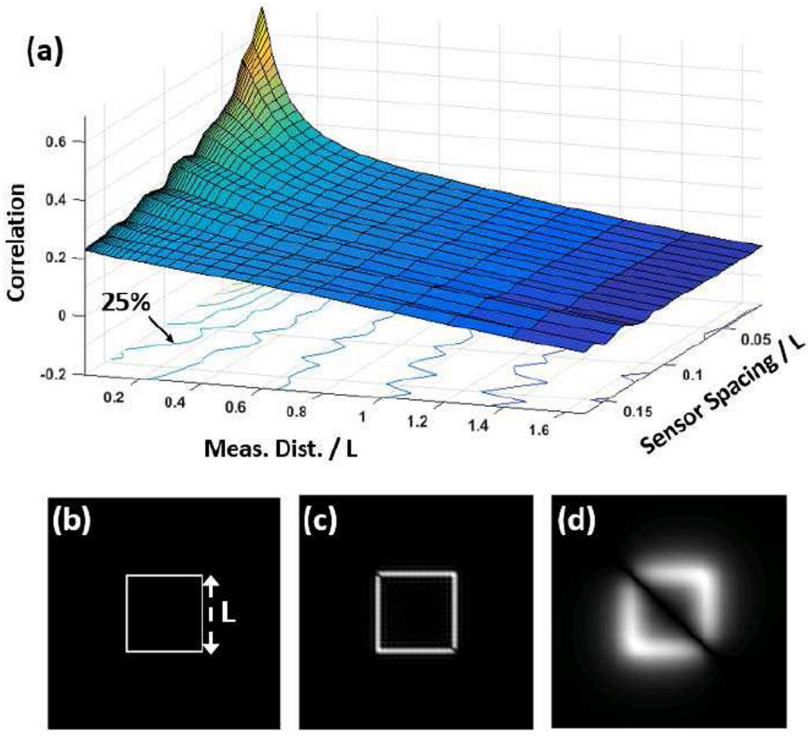

Fig. 13.

The dependency of the constructed current density image quality on the measurement distance (z_0) and array's sensor spacing normalized to the length of the side, ***L***: a) the correlation between the original current carrying trace and the constructed current density image; b) the 1-cm wide original current carrying trace with a side length of 30 cm; c-d) the constructed current density image for a correlation of 70 % and 25 % respectively.

TABLE I

Performance Summary of Magnetic Sensors

	Noise	Upper Sensing Range	3 dB Bandwidth	Operating Temperature	Magnetic Shielding	Principle of Operation
Bell-Bloom [31]	0.1–5 $pT/\sqrt{Hz}$	±10 μT	0.5–10 kHz	20–120 °C	No	Electron Spin Precession
M_x [30]	0.1–5 $pT/\sqrt{Hz}$	±10 μT	0.5–10 kHz	20–120 °C	No	Electron Spin Precession
Pulsed-OPM [this work]	0.1–5 $pT/\sqrt{Hz}$	±10 μT	0.5–2 kHz	120 °C	No	Electron Spin Precession
SERF [19]	0.2–10 $fT/\sqrt{Hz}$	±5 nT	5–300 Hz	150–200 °C	Yes	Electron Spin Precession
Low-T_c SQUID [5]	~3 $fT/\sqrt{Hz}$	NA	~1 MHz	−269 °C	No	Josephson Junctions
Fluxgate [18]	35 $pT/\sqrt{Hz}$	±60 μT	3.5 kHz	Room Temp.	No	Sat. of Ferromagnetic Materials
GMR [17]	0.2 $nT/\sqrt{Hz}$	7 mT	1 MHz	Room Temp.	No	Spin-Dependent Scattering
Hall Effect [10,11]	30 $nT/\sqrt{Hz}$	7 mT	120 kHz	Room Temp	No	Lorentz Force

Note: The performance metrics stated in this table can vary depending on the implementation details; the cited references represent only a single implementation